Prelaunch Radiometric Characterization and Calibration of the S-NPP VIIRS Sensor

Hassan Oudrari, Jeff McIntire, Xiaoxiong Xiong, Jim Butler, Shihyan Lee, Ning Lei, Tom Schwarting, and Junqiang Sun

***Abstract*—The Visible Infrared Imaging Radiometer Suite (VIIRS) is a key instrument onboard the Suomi National Polar-orbiting Partnership (S-NPP) spacecraft that was launched on October 28, 2011. VIIRS is designed to provide top of the atmosphere radiometric measurements and imaging of the entire planet Earth twice daily. It is a wide-swath (3040 km) cross-track scanning radiometer with spatial resolutions of 375 and 750 m at nadir for imaging and moderate bands, respectively. It has 22 spectral bands covering the spectrum between 0.4 and 12.5 μm, including 15 reflective solar bands and 7 thermal emissive bands. VIIRS observations are used to generate 22 environmental data records used by various operational applications and for climate research. This paper describes the prelaunch radiometric calibration and characterization methodologies used by the NASA VIIRS Characterization Support Team, including performance assessments for the reflective and emissive band radiometric calibration, the signal-to-noise ratios, dual gain transition, and dynamic range. Other aspects of the sensor performance such as scattered light response, response versus scan angle, polarization sensitivity, relative spectral response, and crosstalk will also be briefly described. A comprehensive set of performance metrics generated during the prelaunch testing program will be compared to the sensor requirements, and a list of lessons learned will be presented to enhance testing and performance assessment for future Joint Polar-Orbiting Satellite System VIIRS sensors.**

***Index Terms*—Calibration, optical sensors, radiometric, remote sensing, VIIRS.**

I. Introduction

THE Visible Infrared Imaging Radiometer Suite (VIIRS) is a major instrument on the Suomi-National Polar-Orbiting Partnership (S-NPP), a bridge mission between National Aeronautics and Space Administration (NASA) Earth Observing System (EOS) and the Joint Polar-Orbiting Satellite System (JPSS). It is the next-generation polar-orbiting operational environmental imaging sensor with the capability of observing the Earth surface twice a day [1]–[3].

Manuscript received March 7, 2014; revised June 11, 2014; accepted August 19, 2014.

H. Oudrari, J. McIntire, S. Lee, N. Lei, and T. Schwarting are with Sigma Space Corporation, Lanham, MD 20706 USA (e-mail: hassan.oudrari-1@nasa.gov).

X. Xiong and J. Butler are with the Sciences and Exploration Directorate, NASA Goddard Space Flight Center, Greenbelt, MD 20771 USA.

J. Sun was with Aerospace Instruments, Sigma Space Corporation, Lanham, MD 20706 USA. He is now with NOAA/NESDIS/STAR, College Park, MD 20740, USA, and also with Global Science and Technology, Greenbelt, MD 20770 USA.

Color versions of one or more of the figures in this paper are available online at http://ieeexplore.ieee.org.

Digital Object Identifier 10.1109/TGRS.2014.2357678

TABLE I
VIIRS EDRs

Land	
1- Active Fires	2- Snow Cover
3- Land Surface Albedo	4- Vegetation Index
5- Land Surface Temperature	6- Surface Type
7- Ice Surface Temperature	8- Net Heat Flux
9- Snow Ice Characterization	
Ocean	
1- Sea Surface Temperature	2- Ocean Color/Chlorophyll
Imagery and Clouds	
1- Imagery and low light imaging	2- Cloud Top Height
3- Cloud Optical Thickness	4- Cloud Top Temperature
5- Cloud Effective Particle Size	6- Cloud Base Height
7- Cloud Top Pressure	8- Cloud Cover/Layers
Aerosol	
1- Aerosol Optical Thickness	2- Aerosol Particle Size
3- Suspended Matter	

VIIRS incorporates design features from heritage instruments such as the Moderate Resolution Imaging Spectroradiometer (MODIS), the Sea-viewing Wide Field-of-view Sensor (SeaWiFS), and the Advanced High Resolution Radiometer (AVHRR) [4]–[6]. It was designed to provide observations of the Earth with high radiometric quality that would enable better understanding of the global Earth system and its processes. VIIRS was built to replace the current aging satellite systems and to ensure the continuity of the long-term climate data record. Its observations are used to generate a set of 22 environmental data records (EDRs) (see Table I), most of which were initiated by its heritage sensors since the 1980s [7], [8]. The VIIRS sensor is a cross-track scanning radiometer that collects radiometric and imaging data in 22 spectral bands from the visible to thermal infrared wavelength regions ranging from 0.4 to 12.5 μm (see Table II). It has a field of regard of 112.6° in the cross-track direction, and the swath width is approximately 3040 km at a nominal altitude of 828 km. VIIRS was built to meet specifications derived from science requirements and lessons learned from decades of research and calibration on heritage instruments. It was designed with a set of onboard calibrators (OBCs) to assure calibration compliance throughout the mission life. Some of the key VIIRS specifications are shown in Table II.

In 2000, Raytheon Santa Barbara Remote Sensing was officially selected to build the first flight unit of the VIIRS sensor, onboard the S-NPP spacecraft. All of the VIIRS sensor development and testing was completed at the Raytheon facilities between June 2007 and August 2009. The VIIRS

0196-2892 © 2014 IEEE. Personal use is permitted, but republication/redistribution requires IEEE permission.
See http://www.ieee.org/publications_standards/publications/rights/index.html for more information.

TABLE II
S-NPP VIIRS KEY SPECTRAL BAND SPECIFICATIONS

Reflective Solar Bands (RSB)

Band Name	Gain	Center Wavelength (nm)	Bandwidth (nm)	Focal Plane Assembly	FOV (km) Nadir/EOS	Polarization Sensitivity (%)	L_{TYP}	L_{MIN}/L_{MAX}	SNR	Calibration Accuracy @ L_{TYP} (%)
DNB	VG	700	400	DNB	0.8/1.6	NS	3 E-5 (*)	3e-5/200 (*)	6	5/10/30 (**)
M1	HG	412	20	VISNIR	0.8/1.6	3	44.9	30/135	352	2
	LG						155	135/615	316	
M2	HG	445	18	VISNIR	0.8/1.6	2.5	40	26/127	380	2
	LG						146	127/687	409	
M3	HG	488	20	VISNIR	0.8/1.6	2.5	32	22/107	416	2
	LG						123	107/702	414	
M4	HG	555	20	VISNIR	0.8/1.6	2.5	21	12/78	362	2
	LG						90	78/667	315	
M5	HG	672	20	VISNIR	0.8/1.6	2.5	10	8.6/59	242	2
	LG						68	59/651	360	
I1	SG	640	80	VISNIR	0.4/0.8	2.5	22	5/718	119	2
M6	SG	746	15	VISNIR	0.8/1.6	2.5	9.6	5.3/41	199	2
M7	HG	865	39	VISNIR	0.8/1.6	3	6.4	3.4/29	215	2
	LG					3	33.4	29/349	340	
I2	SG	865	39	VISNIR	0.4/0.8	3	25	10.3/349	150	2
M8	SG	1240	20	SMWIR	0.8/1.6	NS	5.4	3.5/164.9	74	2
M9	SG	1378	15	SMWIR	0.8/1.6	NS	6	0.6/77.1	83	2
M10	SG	1610	60	SMWIR	0.8/1.6	NS	7.3	1.2/71.2	342	2
I3	SG	1610	60	SMWIR	0.4/0.8	NS	7.3	1.2/72.5	6	2
M11	SG	2250	50	SMWIR	0.8/1.6	NS	0.12	0.12/31.8	10	2

Thermal Emissive Bands (TEB)

Band Name	Gain	Center Wavelength (nm)	Bandwidth (nm)	Focal Plane Assembly	FOV (km) Nadir/EOS	Polarization Sensitivity (%)	T_{TYP} (K)	T_{MIN}/T_{MAX} (K)	NEdT (K)	Calibration Accuracy @ T_{TYP} (%)
I4	SG	3740	380	SMWIR	0.4/0.8	NS	270	210/353	2.5	5
M12	SG	3760	180	SMWIR	0.8/1.6	NS	270	230/353	0.396	0.7
M13	HG	4050	155	SMWIR	0.8/1.6	NS	300	230/343	0.107	0.7
	LG					NS	380	343/634	0.423	NS
M14	SG	8550	300	LWIR	0.8/1.6	NS	270	190/336	0.091	0.6
M15	SG	10763	1000	LWIR	0.8/1.6	NS	300	190/343	0.07	0.4
I5	SG	11450	1900	LWIR	0.4/0.8	NS	210	190/340	1.5	3
M16	SG	12013	950	LWIR	0.8/1.6	NS	300	190/340	0.072	0.4

Notes:
*: DNB Units are in W/(sr-cm^2)
**: DNB low-gain/ mid-gain/ high-gain
The units of spectral radiance for Ltyp, L_{MIN}, L_{MAX} are watt m^{-2} sr^{-1} μm^{-1}
Dual-gain M-bands have two entries, one for high-gain (HG) and one for low-gain (LG)
The SNR is the minimum (worse-case) required SNR that applies at the end-of-scan
The NEdT is the minimum (worse-case) required NEdT that applies at the end-of-scan
VG: Variable Gain (DNB has three gains, low-gain, mid-gain and high-gain)
SG: Single Gain, NS: Not Specified, EOS: End-of-Scan, FOV: Field of View

instrument then underwent spacecraft-level testing at Ball Aerospace in Boulder (CO), and testing was completed in April 2011.

The NASA VIIRS Characterization Support Team (VCST) is a key member of the larger JPSS government VIIRS independent performance assessment team. This team provided support for the S-NPP VIIRS prelaunch testing to ensure that all sensor performance requirements were well defined. The team also carefully evaluated the VIIRS test program and provided comprehensive analyses of calibration and characterization data sets not only to help understand the VIIRS prelaunch performance but also to produce the required on-orbit calibration lookup tables (LUTs) needed to generate the sensor data records (SDRs) [9].

The purpose of this paper is to provide an overview of the assessment of the S-NPP VIIRS prelaunch radiometric performance based on analysis performed by the NASA VCST. This effort was conducted in close cooperation with other government and contractor teams, including the NASA science team, the Aerospace Corporation, the University of Wisconsin, the Massachusetts Institute of Technology-Lincoln Laboratory, Northrop Grumman Corporation, and Raytheon. In the following sections, we will focus on the main aspects of VIIRS reflective solar band (RSB) and thermal emissive band (TEB)

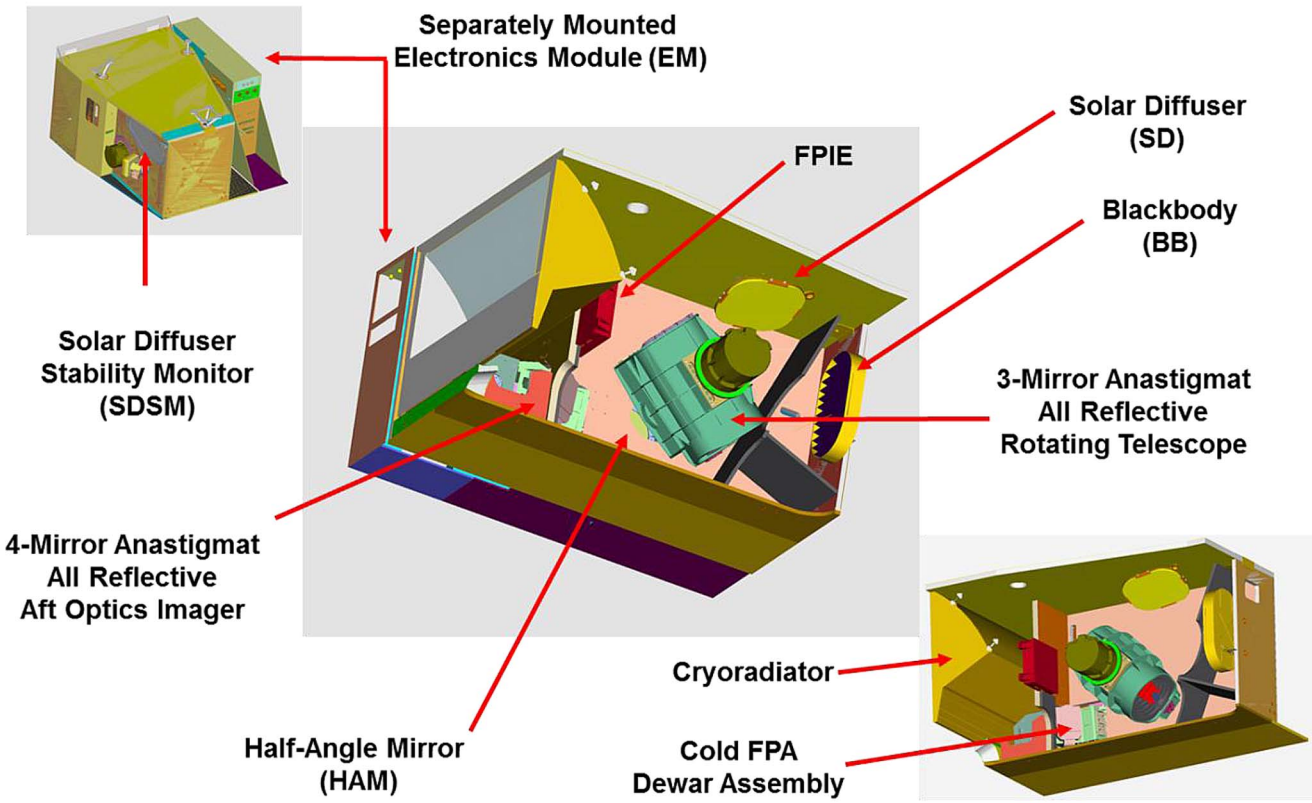

Fig. 1. S-NPP VIIRS sensor design is based on two separate modules—EM and OMM.

prelaunch radiometric performance assessment. The VIIRS day–night band (DNB) radiometric performance and spatial performance assessments are not included in this paper. An overview of the VIIRS sensor design will be presented in Section II. Section III will provide a summary of the VIIRS testing phases followed by a description of the methodologies used to assess the sensor performance in Section IV. Section V will present VIIRS prelaunch performance results associated with RSB and TEB calibration and characterization, as well as a discussion of areas of concern and recommendations.

II. Sensor Design Overview

The VIIRS instrument was built with a strong heritage from the MODIS and SeaWIFS sensors [10], [11], to provide continuous data sets to the Earth science community. Based on inputs generated by a selection of members from the science community and the results from system design studies, a set of performance specifications were generated to design the VIIRS instrument and to identify the on-orbit operations that satisfy the science requirements.

The VIIRS design encompasses numerous technological advances based on the lessons learned from heritage sensors [10], [11]. The OBCs have strong MODIS heritage. These calibrators include the solar diffuser (SD), SD stability monitor (SDSM), and onboard blackbody (BB). The combination of a rotating telescope assembly (RTA) and a half-angle mirror (HAM) is based on a concept developed for SeaWiFS which reduces the instrument response versus scan angle (RVS) effect and stray-light contamination. In addition, the VIIRS HAM rotates at half the speed of the RTA to minimize the Earth rotation effect while the satellite is in motion.

The VIIRS design also incorporates dual gain bands which use detector arrays that can switch between the high and the low gain to provide the necessary sensitivity in the required dynamic range without adding another band. Furthermore, the dual gain bands reduce uncertainties in band-to-band registration and save space on the focal plane. Another design feature is the three-stage pixel aggregation. The VIIRS SDR is generated using 3 to 1, 2 to 1, and 1 to 1 pixel aggregation from nadir to the edge of the scan, which significantly reduces the pixel size growth with the scan angle.

The VIIRS sensor is designed to operate in a polar sun-synchronous orbit with a nominal altitude of 828 km at an inclination angle of approximately 98° relative to the equator [12]. Fig. 1 illustrates the VIIRS sensor design consisting of two modules that are separately mounted to the spacecraft: the optomechanical module (OMM) and electronics module (EM). The OMM contains all of the optical and mechanical assemblies required to collect Earth and calibration data, including the scanning optics, focal planes, and calibration sources. The EM provides all of the electrical interfaces to the S-NPP spacecraft to command and control the VIIRS configuration, to operate the mechanisms in the OMM, and to collect and format the data from the focal planes and transmit them to the spacecraft.

The VIIRS telescope scans the space view (SV) from $-65.83°$ to $-64.97°$, the Earth within $\pm 56.28°$ of nadir, the BB from 99.98° to 100.84°, and the SD from 157.00° to 157.85°, in sequence. The SV, BB, and SD views are collected to support on-orbit instrument calibration and are downlinked

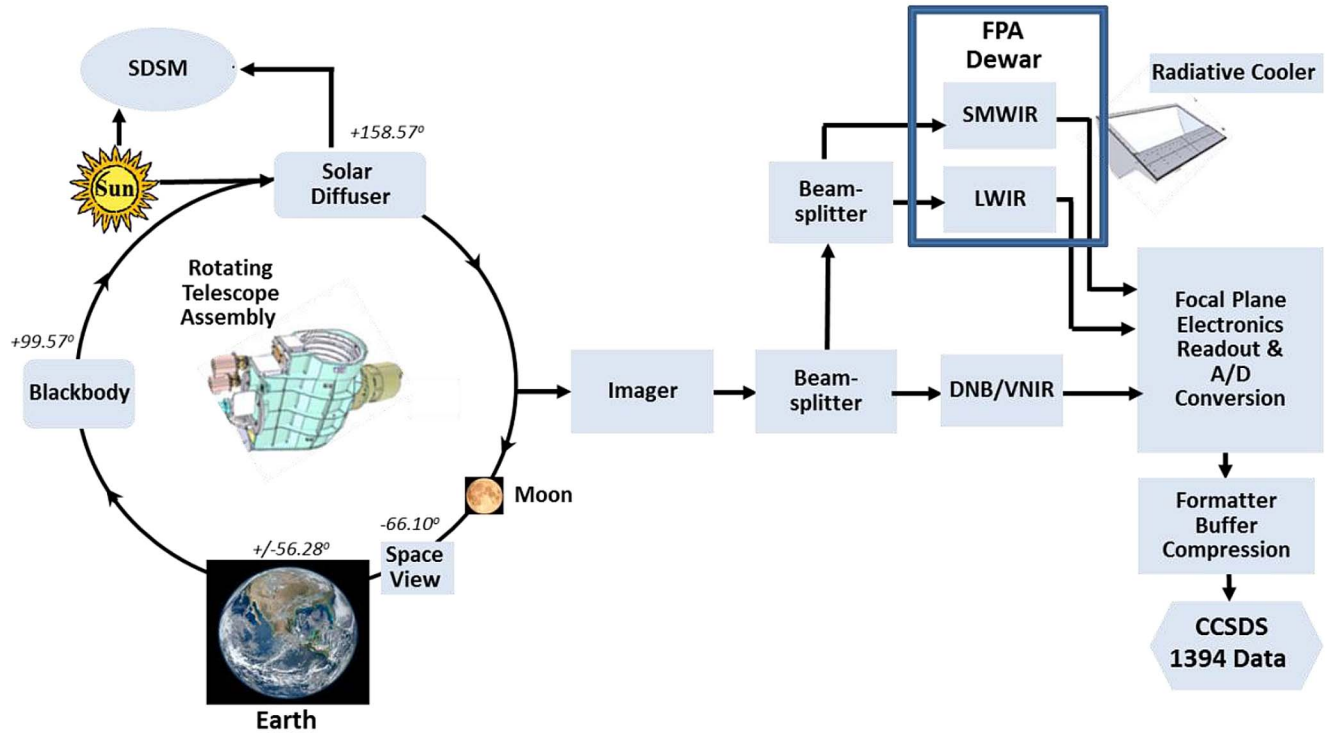

Fig. 2. VIIRS calibration process and data flow.

in the sensor data packets. The rotating telescope scans the Earth's surface which is reflected from the HAM into the aft-optics subsystem. Two dichroic beam splitters direct the light to four different focal plane arrays: the DNB, the visible and near infrared (VisNIR), the short-wave and midwave infrared (SMWIR), and the long-wave infrared (LWIR) focal plane assemblies (FPAs). Both the SMWIR and LWIR are thermally controlled at about 80 K using a passive cryocooler. Light reaching the focal planes' detectors is converted into an analog electric signal, digitized through analog-to-digital conversion, and sent to the sensor data communication stream (see Fig. 2). The instrument temperatures, voltages, and currents are also measured and form the housekeeping telemetry (i.e., health, safety, and engineering telemetry) which are recorded on a scan-by-scan basis.

The detector arrays consist of 16 detectors for each moderate-resolution band (M-band) and 32 detectors for each imaging band (I-band) which are arranged in a linear configuration for the VisNIR bands and are staggered for the SMWIR and LWIR. In what follows, a band's detector 1 is the leading detector in the sensor track direction (instrument detector order). The scanning optics sweep the detector array over the Earth, resulting in the collection of 22 coincident swaths of data (i.e., one per band). The scan interval is synchronized with the spacecraft motion so that the swaths of data taken on successive scans do not leave gaps in the coverage of the Earth's surface.

A. VIIRS OBCs

SD: The SD is a Spectralon diffuser used for RSB calibration when illuminated by the sun, and its bidirectional reflectance distribution function (BRDF) was measured prelaunch. The SD is mounted on the top panel (i.e., opposite to the nadir door) of the VIIRS scan cavity, and its design goal is to generate a uniform Lambertian scene which fills the RTA entrance aperture for each scan. A redesigned SD attenuation screen, incorporating louvers to eliminate earthshine contamination, is used and achieves about 13% transmission at normal incidence to allow the RSB to be calibrated during solar observations.

SDSM: The SDSM is a stand-alone instrument designed to track the BRDF of the SD. It is composed of a 5-cm-diameter integrating sphere embedded with seven silicon detectors equipped with filters that have bandpasses roughly matching the VisNIR M-bands and one detector in the NIR region (935 nm). The SDSM has an optomechanical front end that enables the system to successively view the illuminated SD, a dark cavity, and the Sun. The solar view has a fixed 0.106% transmitting screen to ensure that the SD and solar signal levels are similar. The ratios of the SD and solar view data are used to track the SD BRDF.

Onboard BB: The full-aperture BB has a V-groove design that is black anodized to give an effective emissivity of about 0.996. The BB temperature is measured by six calibrated thermistors. It serves as the TEB calibration source and provides references for dark current dc restoration. In addition to the BB, the scanning of the SV provides background digital numbers per scan line, thereby enabling a two-point radiometric calibration of the seven VIIRS TEBs every 1.85 s. During regular VIIRS operations, the BB is controlled at 292.5 K. However, the BB can be commanded from ambient temperature to 315 K.

B. VIIRS Spectral Bands

RSBs: VIIRS has a total of 14 RSBs (excluding the DNB) located on two separate FPAs. Seven M-bands (M1–M7) and

two I-bands (I1 and I2) are located on the VisNIR FPA; four M-bands (M8–M11) and one I-band (I3) are located on the SMWIR FPA. The VisNIR detector arrays are not temperature controlled and consist of single monocrystalline high resistivity silicon PIN detectors arrayed in nine independent in-track bands spanning the VisNIR spectrum from 0.4 to 0.9 μm. Six VisNIR bands, M1–M5 and M7, are dual gain. The DNB has the capability to capture panchromatic imagery with a broad spectral bandpass covering 0.5–0.9 μm. It employs a backside-illuminated charge-coupled-device detector array operating at $\sim$247 K. The SMWIR bands span the spectral region between 1.2 and 2.25 μm using photovoltaic (PV) HgCdTe hybrid detector arrays operating at 80 K and using microlens arrays to focus energy onto the detectors to improve the signal-to-noise ratio (SNR).

TEBs: VIIRS has a total of seven TEBs located on two separate FPAs. Two M-bands (M12 and M13) and one I-band (I4) are located on the SMWIR FPA; three M-bands (M14–M16) and one I-band (I5) are located on the LWIR FPA. The MWIR bands span the spectrum between 3.7 and 4.1 μm. Similarly to the SMWIR, the LWIR FPA has microlenses and uses PV HgCdTe hybrid detector arrays operating at 80 K with four independent in-track bands spanning the infrared spectrum from 8.55 to 12 μm. The only TEB dual gain band is M13. Both SMWIR and LWIR FPAs are mounted within the cold stage of the sensor dewar equipped with temperature control. One band, M16, is a time-delay-integrated band and has redundant detector arrays, M16A and M16B.

All three FPAs have separate readout integrated circuits to generate amplified readout sent to the EM and have separate integrated filter assemblies to allow spectral measurements with the specified characteristics shown in Table II.

III. VIIRS Testing Overview

The VIIRS instrument completed an intensive ground test program described in the sensor General Test Plan [13] to ensure proper instrument characterization and calibration. This plan describes the integration, functional, and performance tests which were performed on both the engineering development unit (EDU) and the VIIRS Flight 1 (F1) sensor and identifies whether these tests were to be performed before, during, and/or after VIIRS environmental exposure. The work presented in this paper is focused solely on F1 performance testing. However, it is important to stress the crucial role of the lessons learned from the VIIRS EDU and MODIS programs [14]–[16] in enhancing the flight sensor testing design and performance characterization and, in some cases, in helping identify issues early that could have been costly later in the program.

The VIIRS testing program covered the following six prelaunch phases: sensor ambient (June–November 2007), sensor pre-thermal vacuum (TV) (April 2009), sensor TV (May–August 2009), sensor post-TV (September 2009), spacecraft ambient (March 2010), and spacecraft TV (March–April 2011). Comprehensive baseline performance test procedures were executed to characterize the VIIRS instrument over the full range of on-orbit instrument operating conditions, to support the verification of all sensor performance requirements, and to simulate long-term on-orbit performance. These tests also provided the values needed to populate the LUTs upon which the successful execution of the SDR algorithm depends to generate accurate radiance, reflectance, and brightness temperature products. These LUTs capture the prelaunch measured values of the parameters appearing in the radiometric and geolocation equations implemented in the SDR algorithm for different bands, detectors, gain states, HAM sides, electronics configurations, and instrument temperatures [9].

A series of key VIIRS performance tests was performed at ambient, TV, or both. Because of limited space, this paper will focus on key radiometric performance metrics, including the radiometric dynamic range, SNR, noise equivalent delta temperature (NEdT), radiometric response nonlinearity (RRNL), radiometric response uniformity (RRU), relative spectral response (RSR), RVS, scattered light, polarization, and crosstalk. The methodologies used to characterize these radiometric performances are described in more detail in the next section.

IV. VIIRS Testing and Algorithms

This section will provide an overview of the VIIRS characterization and calibration testing in the context of their use in the VIIRS algorithms. Most of the VIIRS algorithms are well defined in the VIIRS sensor performance verification report [17] or in the sensor product requirement document [18]; in some cases, refinements were incorporated by VCST based on the improved understanding of the sensor characteristics and test-related features.

For the RSB and TEB, radiometric calibration parameters such as dynamic range, SNR, RRNL, and RRU of the VIIRS sensor were derived in the TV environment at three instrument temperature plateaus: cold, nominal, and hot. In this paper, only the performance at the nominal plateau (i.e., closest to on-orbit environment) and from B-side electronics (primary electronics) will be reported.

A. RSB Calibration

During instrument level TV tests, a National Institute of Standards and Technology (NIST)-traceable 100 cm diameter Spherical Integrating Source (SIS-100) and a three mirror collimator (TMC) SIS are used as sources with the TMC SIS being a high radiance source used only to characterize the low gain of bands M1–M3. These light sources use multiple lamps with different wattages to generate different radiance levels. For the VisNIR bands, the radiance is tracked using the SIS-100 radiance monitor [14] incorporating both the in-band and out-of-band (OOB) sensor RSRs.

The RSB detected spectral radiance is related to the sensor's digital number by the mathematical form [14]

$$L = \frac{c_0 + c_1 dn + c_2 dn^2}{RVS(\theta_{\mathrm{EV}})}. \tag{1}$$

In (1), the dn is the offset-corrected digital counts. The dark offset used here is the detector digital counts from the SV. The $RVS(\theta_{\mathrm{EV}})$ is the relative HAM reflectance at the angle of incidence θ_{EV}. Since the RSB RVS is very close to unity for

$$y = \frac{2(\tau - 1) \times \left(\frac{c_0}{c_1} + x + \left(\frac{c_2}{c_1}\right) x^2\right)}{1 + 2\left(\frac{c_2}{c_1}\right) x + \sqrt{\left[1 + 2\left(\frac{c_2}{c_1}\right) x\right]^2 + 4\left(\frac{c_2}{c_1}\right) \times (\tau - 1) \times \left(\frac{c_0}{c_1} + x + \left(\frac{c_2}{c_1}\right) x^2\right)}} \tag{3}$$

all angles of incidence (AOIs), we set the RVS to one in the following equations. The goal is to determine the coefficients in (1) using a well-characterized source radiance.

The two sources, the SIS-100 and TMC SIS, are cycled through a series of radiance levels covering the specified dynamic ranges of all RSBs to derive the calibration coefficients. The radiance levels selected for analysis for each band covered the range $[\min(L_{\mathrm{MIN}}, L_{\mathrm{SD}}), L_{\mathrm{MAX}}]$ while excluding saturated data. Here, L_{SD} is the expected spectral radiance for an on-orbit solar observation through the SD.

As noted earlier, because of the uncertainties associated with the sources, the sensor response is determined with and without an attenuator inserted into the optical path at the same source level [13]. The attenuator is an opaque plate with small holes to allow a fraction of light through. Since the time between the two configurations is short (i.e., 2–3 min) for a given source level, the SIS-100 output radiance change is assumed to be negligible. In addition, we assume that the attenuator transmittance does not vary with the SIS-100 power level. Consequently, the ratio of the detected spectral radiances with and without the attenuator is equal to the attenuator transmittance (τ), namely

$$\tau = \frac{c_0/c_1 + dn_{in} + \left(\frac{c_2}{c_1}\right) dn_{in}^2}{c_0/c_1 + dn_{out} + \left(\frac{c_2}{c_1}\right) dn_{out}^2} \tag{2}$$

where dn_{in} and dn_{out} denote the dn with and without the attenuator, respectively. A 3-sigma outlier rejection criterion is used at each stage of the calculation.

To facilitate the data regression, (2) is rewritten as (3) shown at the top of the page, where $x = dn_{\mathrm{out}}$ and $y = dn_{\mathrm{in}} - dn_{\mathrm{out}}$. The model parameters τ, c_0/c_1, and c_2/c_1 are determined through a nonlinear least square regression.

The linear coefficient or gain is determined by inverting (1) and averaging over the selected source levels, namely

$$c_1 = \left\langle \frac{L}{\frac{c_0}{c_1} + dn_{out} + \left(\frac{c_2}{c_1}\right) dn_{out}^2} \right\rangle. \tag{4}$$

The RSB radiometric calibration coefficients are derived at the cold, nominal, and hot TV temperature plateaus for each detector, HAM side, gain stage, and electronic side and are then implemented into the SDR LUTs to support on-orbit calibration [9].

The detector SNR was calculated for each SIS-100 radiance (which is equivalent to the beginning of the scan) by dividing the sample averaged dn over scans by the standard deviation as

$$\mathrm{SNR} = \frac{1}{M} \sum_{j=1}^{j=M} \left[\frac{\frac{1}{N}\left[\sum_{i=1}^{i=N} dn_{i,j}\right]}{\sigma_j} \right] \tag{5}$$

where M and N are the total number of samples and scans, respectively, and i and j are the scan number and sample number, respectively. This approach was more accurate than the one based on scan averaging because the standard deviation of the dn over the samples in a single scan is larger than the standard deviation computed over the scans at the same sample position due to SIS-100 spatial nonuniformity.

To facilitate the computation of the SNR at any radiance level and to smooth out the variability in the SNR over radiance levels, the SNR is fit to the following mathematical form:

$$\mathrm{SNR} = \frac{L}{\sqrt{k_0 + k_1 L + k_2 L^2}} \tag{6}$$

where k_i denotes the fitting coefficients. Equation (6) is a result of the combination of thermal noise, the k_0 term, and Poisson noise, the k_1 term; k_2 is always less than 10^{-6}. This equation is used to derive the SNR and verify requirement compliance.

The RRNL measures the maximum deviation of the test data from a linear polynomial over the range $[L_{\mathrm{MIN}}, L_{\mathrm{MAX}}]$ of a spectral band and is required to be less than 1% [14]. To simplify the computation of this metric, we assume that the quadratic polynomial in (1) accurately describes the detected radiance. In this scenario, the nonlinearity (%) is

$$\mathrm{RRNL} = \frac{100 \cdot |c_2|}{8 \cdot L_{MAX}} \times (dn_{MAX} - dn_{MIN})^2 \tag{7}$$

where dn_{MAX} and dn_{MIN} are the digital counts associated with L_{MAX} and L_{MIN}.

The RRU is the measured detector-to-detector radiance difference when observing a uniform scene. This difference is compared to the noise equivalent delta radiance (NEdL). The RRU at a source radiance L is defined as

$$\mathrm{RRU}(d; L) = \frac{\langle |L(d; L) - \langle L(d; L)\rangle_d| \rangle}{NEdL(d; L)}. \tag{8}$$

In (8), d indicates a particular detector. The spectral radiances are computed via (1), and $NEdL(d, L)$ is the radiance divided by the SNR. In the numerator of the equation, the final average is performed over multiple observations of the same scene. Once S-NPP VIIRS is on orbit, c_1 is computed by observing the SD. As a result, in order to use prelaunch test data to assess the on-orbit RRU, we calculate the RRU with the c_1 computed at the expected SD radiance level using interpolation [14]. For RSB, the maximum RRU per band is required to be less than unity for all scene radiances within $[L_{\mathrm{MIN}}, 0.9L_{\mathrm{MAX}}]$.

B. TEB Calibration

VIIRS thermal band calibration is referenced to a NIST-traceable external BB calibration source (BCS). The radiance reaching the detector (L^*_{BCS}) is the sum of the source radiance as well as contributors along the optical path (i.e., the RTA, HAM, and aft optics), or

$$\begin{aligned} L^*_{BCS} =& \rho_{RTA}\rho_{aft}\rho_{HAM}(\theta_{BCS})\varepsilon_{BCS}L_{BCS} \\ &+ \rho_{aft}\rho_{HAM}(\theta_{BCS})\times[L_{HAM} + (1-\rho_{RTA})L_{RTA}] \\ &+ (1-\rho_{aft})L_{aft}. \end{aligned} \tag{9}$$

The reflectance factors represent the total reflectance of the RTA mirrors, aft optics, and HAM (at the scan angle viewing the BCS). The radiances of the sources are determined via Planck's law convolved over the RSR of each spectral band over the extended bandpass. The temperature of each source is determined from one or more thermistors. Similarly, the at-detector radiances from the onboard BB (L^*_{BB}) and SV (L^*_{SV}) are given by

$$\begin{aligned} L^*_{BB} =& \rho_{RTA}\rho_{aft}\rho_{HAM}(\theta_{BB})\varepsilon_{BB}L_{BB} \\ &+ \rho_{RTA}\rho_{aft}\rho_{HAM}(\theta_{BB})(1-\varepsilon_{BB}) \\ &\times (F_{RTA}L_{RTA} + F_{SH}L_{SH} + F_{CAV}L_{CAV}) \\ &+ \rho_{aft}\rho_{HAM}(\theta_{BB})\left[L_{HAM} + (1-\rho_{RTA})L_{RTA}\right] \\ &+ (1-\rho_{aft})L_{aft} \end{aligned} \tag{10}$$

$$\begin{aligned} L^*_{SV} =& \rho_{aft}\rho_{HAM}(\theta_{SV})\left[L_{HAM} + (1-\rho_{RTA})L_{RTA}\right] \\ &+ (1-\rho_{aft})L_{aft}. \end{aligned} \tag{11}$$

In ground testing, a cold reference target is used to simulate the deep space view; as a result, the source radiance in the SV is negligible. In addition, there is a contribution from light reflected off the BB into the path; the relative contributions of the RTA, the BB shield (SH), and the cavity (CAV) are denoted by F_{RTA}, F_{SH}, and F_{CAV}, respectively.

The path difference radiance between two sources, the latter of which is the SV, is then

$$\begin{aligned} \Delta L_{BCS} =& RVS_{BCS}\varepsilon_{BCS}L_{BCS} \\ &+ \frac{(RVS_{BCS} - RVS_{SV})}{\rho_{RTA}}[L_{HAM} + (1-\rho_{RTA})L_{RTA}] \end{aligned} \tag{12}$$

$$\begin{aligned} \Delta L_{BB} =& RVS_{BB}\varepsilon_{BB}L_{BB} + RVS_{BB}(1-\varepsilon_{BB}) \\ &\times (F_{RTA}L_{RTA} + F_{SH}L_{SH} + F_{CAV}L_{CAV}) \\ &+ \frac{(RVS_{BB} - RVS_{SV})}{\rho_{RTA}}[L_{HAM} + (1-\rho_{RTA})L_{RTA}]. \end{aligned} \tag{13}$$

Note that the aft-optics radiance contributions have cancelled as they are common to both paths and that the path difference radiance was renormalized by the product of the RTA and aft-optics reflectance factors. The absolute value of the HAM reflectance (at the SV scan angle) has been also cancelled; what remains is the scan-angle-dependent relative reflectance of the HAM (referred to as the RVS).

The path difference at-detector radiance is modeled as a quadratic polynomial in the offset-corrected digital response, or

$$\Delta L = c_0 + c_1 dn + c_2 dn^2. \tag{14}$$

The external and internal BBs are cycled through a series of temperature levels; the data acquired are used to determine the coefficients using a least squares fit of the at-detector radiance to the detector response. The sensor specification defines the dynamic range over which each VIIRS thermal band must be calibrated. In this paper, the dynamic range was optimized to include all available data not contaminated at high temperature by saturation and for which the SNR was greater than one at low temperature. An additional correction to the external BB at-detector radiance (not shown) was included to account for any drifting in the detector gain during the course of the test by referencing to the internal BB.

The retrieved EV radiance for the BCS is determined by inverting (12), or

$$\begin{aligned} L_{BCS-ret} =& \frac{\left(c_0 + c_1 dn_{BCS} + c_2 dn^2_{BCS}\right)}{RVS_{BCS}} \\ &- \frac{(RVS_{BCS} - RVS_{SV})}{RVS_{BCS}\rho_{RTA}}\left[L_{HAM} + (1-\rho_{RTA})L_{RTA}\right]. \end{aligned} \tag{15}$$

The low gain state of band M13 (high temperature) cannot be calibrated using the BCS like the high gain state, so a second high-temperature external BB (TMC BB) was used. The TMC BB uses mirrors to collimate thermal radiance from a BB and can reach a maximum temperature of about 750 K, while the BCS can only reach 345 K. The calibration of the TMC BB was tied to the BCS by cross-calibration at lower scene temperatures where both sources overlap. This calibration was then extended to the high-temperature region, using

$$\begin{aligned} \Delta L_{TMCBB} =& RVS_{TMCBB}\varepsilon_{TMCBB}L_{TMCBB} \\ &+ RVS_{TMCBB}(1-\tau_{TMC})L_{TMC} \\ &+ RVS_{TMCBB}(1-\rho_{window})L_{window} \\ &+ \frac{(RVS_{BB} - RVS_{SV})}{\rho_{RTA}} \\ &\times \left[L_{HAM} + (1-\rho_{RTA})L_{RTA}\right]. \end{aligned} \tag{16}$$

Because the TMC BB is located outside the TV chamber, additional source terms in the TMC BB path were included for the TMC optics and the TV chamber window. The transmission of the TMC optics was used to facilitate the calibration transfer from the BCS to the TMC BB.

The radiometric sensitivity was determined by fitting the SNR to the at-detector source radiance using (6). The BCS spatial stability and temporal stability were high; thus, the SNR results were closer to the true sensor SNR.

The NEdT is the fluctuation in the scene temperature equivalent to the system noise and is computed via

$$\mathrm{NEdT} = \frac{\Delta L_{BCS}}{\mathrm{SNR}\frac{\partial L}{\partial T}}. \tag{17}$$

The derivative is of Planck's law with respect to the source temperature. The NEdT was determined at all source levels but is required to be below a specified threshold only at T_{TYP}; this was determined using the fit SNR and at-detector radiance.

The RRNL is defined for the thermal bands as

$$\mathrm{RRNL} = \frac{\max(\Delta_{fit})}{L_{MAX}} \tag{18}$$

where the numerator is the maximum fitting residual over the dynamic range for a linear fit. The sensor requirement is that the RRNL should be less than 1%.

The absolute calibration uncertainty includes all the uncertainties associated with the calibration. This is beyond the scope of this paper; however, the fit uncertainty contribution to the absolute uncertainty is analyzed using the absolute radiance difference (ARD), or

$$\mathrm{ARD} = 100\frac{L_{BCS-ret} - L_{BCS}}{L_{BCS}}. \tag{19}$$

This is the percent difference between the retrieved and BCS radiances with the ARD essentially being a measure of the fit uncertainty's effect on the accuracy of the retrieved radiance. This requirement is compared against the specification values listed in the sensor specification document [18], and from which the specification values at L_{TYP} are listed in Table II.

The RRU defines the detector-to-detector uniformity or striping as described in (8). The sensor specification is met if the RRU is less than unity within the radiance range from L_{MIN} to $0.9L_{\mathrm{MAX}}$.

C. Other Sensor Performance Testing

Scattered Light: The VIIRS scattered light performance has two parts: near-field response (NFR) and the far-field stray light. NFR is defined as scattered light within 4° from the RTA line of sight, and far-field stray light is defined as a region from 4° to 62.5° where there is no direct and predictable path from the source to the detectors.

A scatter measurement assembly (ScMA) was used to measure the instrument NFR. The ScMA consists of a high energy tungsten filament source for the RSB and a heated ceramic glowbar source for the TEB. The source is collimated before passing through a slit slightly smaller than the width of one M-band detector. Bandpass filters were used to minimize crosstalk contamination in the measured NFR. Neutral density filters were used to measure the response near the slit and scale the near-field measurements made without the neutral density filter. The two measurements were combined to provide the total NFR.

The VIIRS NFR requirement is defined as structured scene performance specified as the maximum allowable response at a specified angle limit coming off a 20 × 20 km bright target for each band. To estimate the structured scene response, a Harvey–Shack BRDF scattering model [18] was used to fit the measured NFR profile and remove test artifacts and noisy samples. The fitting was conducted in four regions separated by response peak and baffle locations. The NFR profiles were convoluted to simulate the structured scene response from a bright target as described in the sensor NFR requirement [13].

The far-field stray-light test was performed using a radiometrically calibrated 1000-W studio lamp. The VIIRS telescope was staring at a cavity-type BB while the lamp was moved through 33 equally distanced hemispherical positions to evaluate the angular stray-light distribution. The lamp positions covered a roughly equally divided annulus out to 62.5° off nadir to simulate the Earth as subtended by VIIRS at the S-NPP on-orbit operating altitude. The measured instrument response was scaled by the ratio of the studio lamp irradiance and a model of bright cloud irradiance. The VIIRS far-field stray-light requirement uses a worse case hole-in-the-cloud scenario. The measured instrument response at each position was weighted by the corresponding annulus and then aggregated to estimate the total stray-light contribution from the specified worse case scenario. The test was conducted with the RTA locked at SV, nadir, and the end of the scan to obtain stray-light estimates at different scan angles.

RVS: The RVS test characterizes the relative reflectance of the HAM as a function of AOI. Testing was performed during the ambient phase for the RSB using the SIS-100 and for the TEB using a cavity-type BB and the onboard BB. Data taken at 11 AOIs for RSB and 12 for TEB were used to fit the RVS function, which is a quadratic polynomial in AOI, after corrections for source drift and background radiances were performed.

Polarization Sensitivity: VIIRS sensitivity to polarized light was initially measured during ambient phase testing and then retested in the post-TV phase because of repeatability issues of the polarized source used in the ambient phase. Polarization sensitivity was characterized in the 400–900-nm range covering bands M1–M7, I1, and I2. An integrating sphere combined with a sheet polarizer was used during the post-TV phase to provide polarized light at seven different scan angles. The sheet polarizer was mounted on a rotary stage and was rotated in 15° increments from 0° to 360°. Two sheet polarizers were used during testing: one for bands M1–M6 and I1 and the other for bands M7 and I2. Additionally, a long wavelength spectral blocking filter was placed in the optical path when measuring the short wavelength bands, M1 to M3, to eliminate near infrared OOB contributions.

RSR: The RSR of all VIIRS bands was measured with VIIRS in TV using a double monochromator operating in subtractive mode. The monochromator exit slit image was aligned to illuminate one spectral band at a time or one set of staggered detectors at a time, and the spectral response was measured by stepping the monochromator wavelength over a spectral region covering roughly the acceptance of the dichroic spectral bandpass. The monochromator output was characterized using a reference detector located near the exit slit outside of the TV chamber. The VIIRS spectral data collected were corrected for the source spectral shape and normalized to the peak response to determine the VIIRS RSR. The data were analyzed to

determine each band's center wavelength, full-width at half-maximum bandwidth, 1% peak response points, and ratio of OOB to in-band radiance from a modeled source employing the combination of the reflected solar radiance off the Earth and the emission of the Earth.

The VisNIR-band RSR was measured in TV from 350 to 1100 nm at a nominal 5.5-nm OOB step size and at slightly smaller step sizes for the in-band response. These measurements were combined with the RSR measurements performed using the NIST Traveling-Spectral Irradiance and Radiance responsivity Calibrations using Uniform Sources (T-SIRCUS) [19] in spacecraft-level ambient testing. These resulting detector-based hybrid RSRs were processed to make the band average RSRs used in the postlaunch SDR LUTs [9], [20]. The T-SIRCUS testing covered wavelengths from 390 to 1000 nm with increased spectral resolution and at irregular and slightly smaller step sizes than the TV measurements. The T-SIRCUS measurements were performed with flood illumination on the FPA, so the measurement includes optical and electrical crosstalk effects in addition to OOB response.

The short-wave infrared (SWIR) and TEB RSRs were measured exclusively during sensor-level TV testing. Midwave infrared (MWIR) bands were measured over the same range as that of the SWIR (i.e., from 1000 to 7100 nm), while the LWIR bands were measured from 1.8 to 16.1 μm. From this test, band average RSRs were produced that went into calculating the RSR LUTs for the SWIR and the BB radiances used in the SDR LUTs for the TEB [9].

Crosstalk Performance: S-NPP VIIRS crosstalk requirements were very stringent compared to those from heritage sensors such as MODIS. They require that, for a receiver detector, the total received signal should not exceed the maximum of 0.2% L_{TYP} and 0.5 NEdL when all other detectors are illumined with L_{MAX} radiance. For this reason, the major goal of the VIIRS prelaunch crosstalk analysis was not to verify the compliance with the requirements but to have good quality test data to assess the magnitude of crosstalk and to generate a comprehensive characterization.

Two baseline crosstalk tests were conducted, one in ambient and the other in TV. For each focal plane, the ambient crosstalk test measured the detector-to-detector static crosstalk for all sender–receiver pairs as well as the dynamic crosstalk using four different reticles. All reticles provided strong contrast in the sender signal and showed good sensor performance for the dynamic crosstalk. In the TV chamber, the band-to-detector optical crosstalk was tested using a double monochromator for all bands, and the band-to-detector static crosstalk was tested using the same source with in-band light for the sender. These comprehensive tests were used to provide crosstalk magnitude estimates and the crosstalk influence coefficient (IC) maps needed for SDR impact assessment and modeling.

The optical crosstalk, in terms of ICs, is the ratio of the receiver radiance L_R to the radiance output by the monochromator, L_{mono}, as

$$IC(B_S,B_R,D_R,SF_R,\lambda_{mono})=\frac{L_R(B_S,B_RD_R,SF_R,\lambda_{mono})}{L_{mono}(B_S,\lambda_{mono})} \tag{20}$$

where B, D, SF, and λ represent a given band, detector, subframe (I-bands only), and wavelength, respectively, and the subscripts S and R denote the sender band (or illuminated band) and the receiver band, respectively. One thing to note about (20) is that it relates crosstalk on a band-to-detector basis—for a given sender, B_s, the receiver element is a given subframe of detector D_R in band B_R. These ICs were calculated for each wavelength, averaged based on predefined spectral bins and then averaged over detectors to generate a band-to-band crosstalk map.

Since the specification as written was both difficult to test and very difficult to meet, an intensive effort was put on crosstalk characterization and the generation of complete crosstalk maps to assess the impact on SDR and EDR products.

V. Results

The analysis of VIIRS test data allowed the generation of RSB and TEB calibration coefficients and the verification of sensor performance requirements. These VIIRS sensor requirements have levied several radiometric calibration and stability requirements to ensure high quality radiance products. This section will describe the VIIRS analysis assessments showing how VIIRS performance compares against the sensor requirements.

A. RSB Calibration

Calibration, SNR, Dynamic Range, Linearity, Uniformity, and Gain Transition: A set of dn_{out} and $dn_{\mathrm{in}} - dn_{\mathrm{out}}$ obtained from instrument level TV tests covering a series of spectral radiance levels is fit to (3). The offset c_0/c_1 for most RSBs (i.e., both high and low gains for dual gain bands) has a magnitude of less than 0.3 which is comparable to its standard deviation with the exception of a few RSBs. c_0/c_1 is about -1.0 for M1 and M2 high gain and is about 0.2 to -0.6 for low gain, whereas its standard deviation is about 0.2 to 0.3, indicating a possible negative computed spectral radiance at very low dn. However, the dn at L_{MIN} for M1 is about 400 (i.e., high gain) and is much larger than the c_0/c_1; the same is true for M2. The value of c_0/c_1 is about -2.0 for the I3 band, which is much larger than the standard deviation of about 0.3. As in case of M1 and M2, the dn at L_{MIN} for I3 is about 60, which is much larger than the offset c_0/c_1. The quadratic term c_2/c_1 has values ranging between -2×10^{-6} and -3×10^{-6} for all RSBs except I3, which has c_2/c_1 values of about 3.5×10^{-6}. The standard deviation of c_2/c_1 is on the order of 10^{-7}.

As noted earlier, the detected spectral radiance relates to the sensor's digital number in the mathematical form of (1). Based on this formulation and the subsequent algorithms described in Section IV-A, the performance metrics for the RSB are plotted in Fig. 3 using data taken from TV nominal plateau tests for electronics side B and HAM side A. Other instrument conditions give similar results unless otherwise stated. The ratios of the calculated to the specified SNR at L_{TYP} are plotted in Fig. 3 (top plot) for all RSBs. The figure shows clearly that all RSBs have SNRs at L_{TYP} that are larger than the requirements. The smallest and largest margins are 31% and 2383% for bands M5 high gain and I3, respectively. The SNR

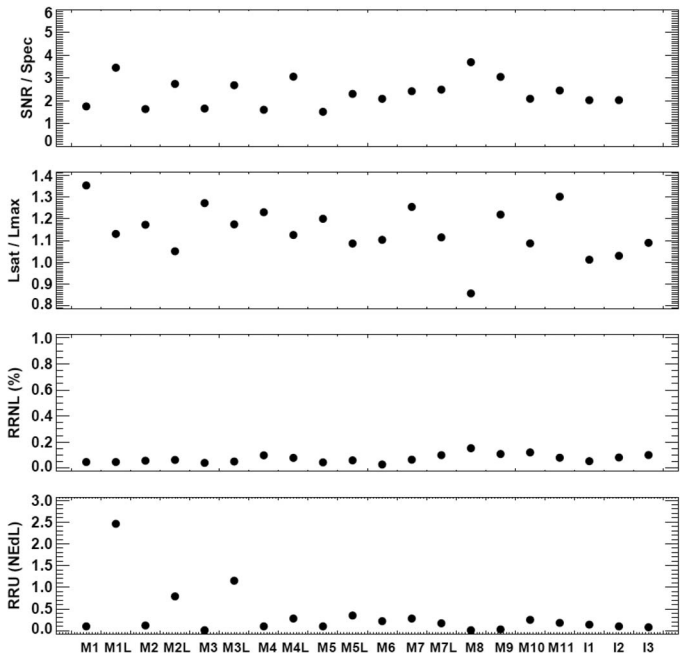

Fig. 3. RSB key performance metrics measured in TV at nominal plateau: SNR, dynamic range, nonlinearity, and uniformity, derived as the mean values of all detectors within a band.

value for I3 is not shown in the plot due to the exceptionally large value. Fig. 3 (second plot) shows the ratio of the calculated L_{SAT} to the specified L_{MAX} for each band. All RSBs saturate higher than L_{MAX}, except M8 which saturates at around 85% of L_{MAX}. Even though M6 met its dynamic range requirement, frequent saturation is expected on orbit because of its low L_{MAX} (single gain), leading to rollover in the response that needs to be flagged in the SDR products. The mean RRNL values for all RSBs are shown in Fig. 3 (the third plot) and are clearly compliant with the specification of 1.0% with significant margins. Meeting the detector-to-detector uniformity (RRU) requirement of 1.0% over the full dynamic range as described in Section IV-A was a major challenge for the VIIRS RSB because the sensor has excellent noise performance for all RSBs. In addition, the source uniformity is a possible major contributor to these noncompliances. Therefore, some of the detector-to-detector scene striping in a band could be mitigated on orbit by using the SD calibration data. Although meeting the RRU requirement over the entire dynamic range is challenging, at L_{TYP}, all RRUs for the dual gain bands meet the specification of RRU less than 1.0%, except the low gain for M1 and M3 (see Fig. 3, bottom plot). When the spectral radiance is increased to L_{MAX}, the RRUs derived for the dual gain bands are compliant with the specification at high gain and noncompliant at low gain. At L_{MAX}, all single gain band RRUs are noncompliant with the specification except M6, M11, and I3. The maximum RRU is about 10.4 for M1 in low gain.

The dual gain bands' transitions were tested using partial views of the SIS-100 source to more accurately determine the radiance at which the electronics switches from high to low gain. The measured dual gain transitions for the RSBs M1–M5 and M7 are shown in Fig. 4. The ratio of the measured to the specified transition radiance is plotted. The requirement states that the transition should occur between 0% and 50% of the high gain L_{MAX} for bands M1–M2 and between 0% and 20% for bands M3–M5 and M7. The upper and lower specified limits for each band are shown in Fig. 4 as solid lines. The band average transition values all fall within the specified limits. One radiometric anomaly affecting all dual gain bands is associated with an increase of noise magnitude (up to four times) and nonlinearity at a small region of the dynamic range located at about 10% below the radiance at which the gain transition occurs. An algorithm was developed to flag these anomalies in the SDR products.

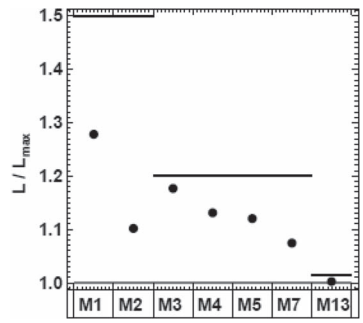

Fig. 4. Ratio between actual radiance transition and transition requirement for VIIRS dual gain bands. (Dots) Ratios less than the (solid line) specification indicate compliance with specification.

It is crucial to note that, for the VIIRS RSB, the requirements on the absolute radiometric calibration are against the spectral reflectance accuracy of 2% when viewing a uniform unpolarized scene of typical radiance, L_{TYP}. This uncertainty verification was performed using contributors which have been constrained by sensor-level requirements while others are based on the sensor contractor allocations [17]. A contributor to the spectral uncertainty includes the detector response characterization uncertainty, which states that the response of a detector to a range of radiance levels from L_{MIN} to L_{MAX} must be fit with a second degree polynomial to within 0.3%. This characterization uncertainty requirement was also very challenging for the VIIRS RSB to meet, but the spectral reflectance accuracy (2%) was met for all RSBs except M11 (2.8%) due to its very low L_{TYP} value [17].

B. TEB Calibration

Calibration, NEdT, Dynamic Range, Gain Transition, Linearity, and Uniformity: The thermal bands were fit using a quadratic polynomial as described in (14) for all high gain bands and all detectors. The radiance residual is generally less than 1.0% for the LWIR bands I5 and M14–M16. The residuals for I4, M12, and M13, in particular, increase at lower temperatures (i.e., up to 10% at T_{MIN}); these bands are known to exhibit greater nonlinearity at low radiances. In addition, detector 1 in band M12 exhibited out-of-family radiometric response with respect to other M12 detectors.

The offset calibration coefficient c_0 is generally small, on the order of 10^{-2} or less. This indicates that the model is generally consistent with an offset of zero. However, the added degree of freedom is useful in constraining the data. The nonlinear term (c_2) is also very small, on the order of 10^{-8} or less, which indicates that the instrument has a very linear response to the

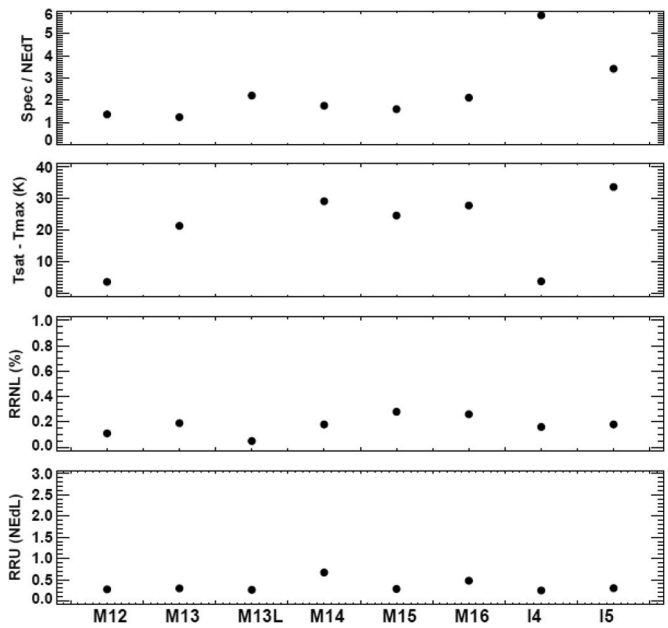

Fig. 5. TEB key performance metrics measured in TV at nominal plateau: NEdT, dynamic range, nonlinearity, and uniformity, derived as the mean of all detectors within a band. M13 low gain saturation was not measured.

input radiance. The nonlinear term is negative for all the MWIR bands and positive for all the LWIR bands. Thus, the curvature of the fit is opposite from the MWIR to LWIR bands. The linear term (c_1) is dominant for all the thermal bands. There is some odd–even detector dependence in the gain for bands I5, M12, and M13. Also, the gains tend to decrease with the detector number for the LWIR bands I5 and M14–M16.

For M13 low gain, c_0 exhibits large variations around zero. Also, the gain is much lower for the high gain bands, with $c_1 \sim 0.14$ for low gain and $c_1 \sim 0.0017$ for high gain. This is necessary in order for M13 to access scene temperatures up to ~634 K without saturating. Even though the gain is very low, the linear term still dominates (i.e., $c_2 \sim 10^{-7}$), indicating that the response is very linear with input radiance.

The band average ratios of the specified to the measured NEdT at T_{TYP} are plotted in the top plot in Fig. 5. All emissive bands and detectors are well below the NEdT at T_{TYP} specification, including M13 low gain. M14 shows the closest margin to the specification, which is about 35%. In general, the variation with the detector is small. The exceptions are detector 31 in I5, detector 1 in M12, and detector 8 in M16A, all of which are out-of-family. As expected, the lower (higher) the temperature, the higher (lower) the NEdT. For the LWIR, the NEdT is below 1.0 K, even at the lowest scene temperatures; for the MWIR, the NEdT increases to around 1.0 K for M12 and M13 and roughly 3.5 K for I4 at 230 K. The NEdT for the M13 low gain for all detectors is well below the specification.

The saturation brightness temperature is plotted in the second plot in Fig. 5, as a ratio to the specified T_{MAX} for each band, and shows all TEB saturation above the specified limits. All of the LWIR bands digitally saturate first, while the MWIR bands I4 and M12 show electronic saturation first. Higher input radiance than L_{MAX} for these two bands resulted in decreasing detector response, appearing as a response rollover and occurring above about 358 K. Saturation was not observed during prelaunch testing for M13 low gain due to test limitations.

All bands pass the nonlinearity requirement (less than 1%) as shown in the third plot in Fig. 5; M14 has the closest margin at about 60%. The nonlinearity is very consistent over detectors and HAM sides. The RRNL for M13 low gain for all detectors is well below the specification.

The detector-to-detector striping specification, requiring the RRU to be less than 1, applies only between the specified L_{MIN} and $0.9L_{\mathrm{MAX}}$. The band average RRU at L_{TYP} is shown in the bottom plot in Fig. 5. All high gain bands meet this requirement with the exception of M14 at high scene temperatures. The RRU generally increases with scene temperature, particularly for bands M12, M13 high gain, M14, and M15. The RRU is essentially a measure of the detector-to-detector uniformity in the retrieved radiance in relation to the NEdL and is an indicator of whether the striping is within the noise. The RRU is greater than one for M14 above 327 K. In addition, M13 and M15 approach the specification value at high scene temperatures. The worst case M13 low gain detector uniformity is well below the noise over the optimized dynamic range.

The ARD for the I-bands has a specified limit of 5.0% (2.5%) for I4 (I5) at a scene temperature of 267 K. This requirement is assessed at the nearest measured scene temperature, 269.9 K. Both I-bands pass the specification with large margins. For the M-bands, the requirement is stratified at four scene temperatures for M12 and M13 and at five scene temperatures for M14–M16. Again, the nearest measured scene temperature to the specified scene temperatures is used to assess the requirement. In all cases, the worst case ARD is well below the specified value. The ARD for all LWIR bands is less than 0.2% above 230 K; this indicates that the fitting contribution to the radiance retrieval is very accurate for these bands. In contrast, the MWIR bands I4, M12, and M13 have an ARD between 0.3% and 0.7% above a scene temperature of 270 K; below 270 K, the MWIR ARD tends to increase dramatically. The MWIR bands are known to exhibit nonlinear behavior, particularly below 270 K; the behavior observed in the ARD is the result of fitting residual error in the calibration coefficients. In addition, the MWIR bands are consistently offset by about 0.3%; this results from the scan-by-scan BB correction in the retrieved radiance. The worst case M13 low gain retrieval error (i.e., ARD) is less than ~0.5% at the low end of the dynamic range and less than 0.2% above 450 K. It should be pointed out that there is no ARD specification for M13 low gain.

The M13 band-averaged gain transition radiances are plotted in Fig. 4 relative to the specified transition radiance. M13 is specified to transition between 343 K and 348 K. For all cases, the calculated scene temperatures for both hot and nominal plateaus meet the requirement. However, at the cold plateau, all even detectors and some odd detectors transition at scene temperatures above 348 K. The difference over detectors within a given plateau is ~2 K, and the difference over plateaus is ~4 K. Thus, the gain transition varies over instrument conditions and detectors by ~6 K. As a result, M13 cannot meet the requirement for all instrument conditions tested; the noncompliances hold for both electronics sides and are considered as low risk to SDR and EDR products.

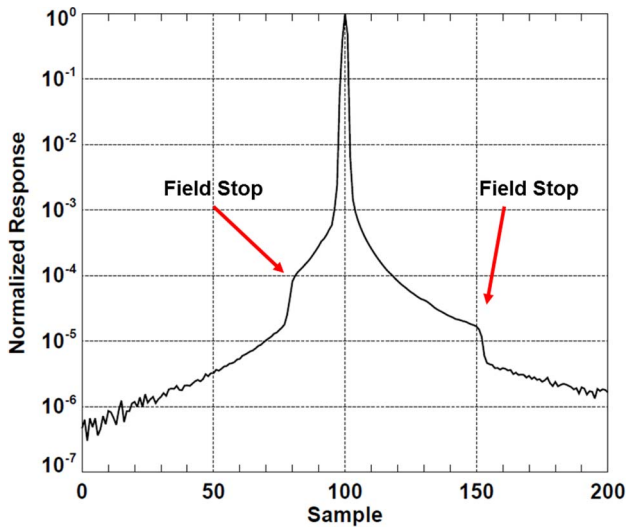

Fig. 6. Measured near-field response for band M5 (672 nm) detector 8, as a function of samples. The figure also shows the location of the field stops.

C. Other Performance Testing

Scattered Light: As described in Section IV-C, the VIIRS F1 scattered light was evaluated by two separate tests, NFR and far-field stray-light rejection. Each test has its own set of requirements.

Fig. 6 shows the normalized response for band M5 detector 8 and represents a typical profile observed in the VIIRS NFR measurements when the sensor is scanning the source through a vertical slit reticle. The figure shows the NFR falling off rapidly from the peak with additional sharp drops seen around the field baffle locations. In this example, the M5 NFR drops to about 0.1% within five samples of the peak (i.e., corresponding to approximately 1.25 km at the Earth surface), and the field baffle reduces the NFR by about one order.

The NFR is estimated for each detector, and the results show good detector uniformity within the same band. The NFR requirement states that the maximum allowable scattered radiance, as a fraction of typical scene radiance, from a bright target at the specified angular distance shall be less than the specified value. The band-averaged VIIRS NFR performance is summarized in Table III, including the bright target radiance (L_{bright}), the specification (L_{spec}), and the ratio $L_{\mathrm{scat}}//L_{\mathrm{spec}}$. The results show that all VIIRS bands meet the specification ($L_{\mathrm{scat}}/L_{\mathrm{spec}} < 1$) with a margin, except M15 and M16, which are ~25% below the requirement.

Table IV shows the estimated S-NPP VIIRS far-field stray-light compliance, including some intermediate parameters used to compute the final stray-light assessment. The sensor test data analysis showed that all RSBs meet the stray-light requirement with large margins, with the exception of M11 which was 3.8 times the specification. M11 failed the specification due to the very low $L_{\mathrm{TYP}}(L_{\mathrm{TYP}} = L_{\mathrm{MIN}})$, although the estimated stray light in percent is comparable to that of other bands. Excluding M11, all RSBs meet the specification with margins between 41% and 85%. Test analysis has shown that stray light is strongly dependent on the source angle relative to the VIIRS viewing direction and is largely negligible when the source-to-view angle is larger than 26°. Furthermore, at the same angle, stray light is slightly larger along the track direction than along the scan.

TABLE III
SUMMARY OF VIIRS NFR PERFORMANCE

Band	Center Wavelength (nm)	Angular Separation (mrad)	L_{bright}	L_{spec}	L_{scat} / L_{spec}
M1	412	6	162	2.77E-03	0.39
M2	445	6	180	2.22E-03	0.45
M3	488	6	160	2.00E-03	0.50
M4	555	6	160	1.31E-03	0.47
M5	672	6	115	8.70E-04	0.63
M6	746	12	147	1.31E-03	0.12
M7	865	6	124	5.16E-04	0.90
M8	1240	6	57	9.47E-04	0.62
M9	1378	NA	NA	NA	NA
M10	1610	6	86.1	8.48E-04	0.76
M11	2250	6	1.2	1.00E-03	0.42
M12	3700	3	0.3	1.67E-03	0.64
M13	4050	3	1.7	1.86E-03	0.63
M14	8550	NA	NA	NA	NA
M15	10763	3	12.5	7.75E-04	**1.25**
M16	12013	3	11.3	7.92E-04	**1.26**

TABLE IV
SUMMARY OF VIIRS F1 STRAY-LIGHT PERFORMANCE

Band	E_{Earth}	L_{TYP}	dn_{spec}	dn_{stray}	dn_{stray} / dn_{spec}
M1	1444.1	44.9	17.016	2.583	0.152
M2	1526.1	40	9.385	2.534	0.27
M3	1563.5	32	8.809	2.557	0.29
M4	1510.7	21	7.53	2.388	0.317
M5	1265.7	10	5.055	2.379	0.471
M6	1088.9	9.6	8.001	3.616	0.452
M7	833.2	6.4	6.871	4.059	0.591
M8	353	5.4	1.454	0.77	0.53
M9	262.9	6	2.437	0.915	0.376
M10	165.7	7.3	3.554	1.295	0.364
M11	56.4	0.12	0.11	0.415	**3.778**
I1	1341.3	22	1.017	0.26	0.255
I2	833.2	25	2.512	0.385	0.153
I3	165.7	7.3	3.188	0.787	0.247

E_{Earth} = Irradiance of the cloud covered Earth scene
dn_{spec} = dn at 1 % of typical radiance (L_{TYP})
dn_{stray} = dn associated with measured stray light

RVS: Fig. 7 shows the band-average RVS functions using data from HAM side A. For all bands, the RVS differences between HAM sides are small with the exception of band M6. The variation in the RSB RVS for M1–M11 and I1–I3 is generally small as shown in the top and middle plots, varying by less than 1% over the full operational AOI range of 28.6°–60.2°. The RSB RVS uncertainty requirement was 0.3% which was determined here as the fitting residuals. All RSBs had uncertainties lower than 0.15%, except for band M9 which had 0.43%. The determination of band M9 RVS was complicated due to water vapor fluctuations during RVS testing.

The band-averaged RVS for the MWIR bands, M12, M13, and I4, and the LWIR bands, M14–M16 and I5, are plotted respectively in the middle and bottom plots of Fig. 7. The

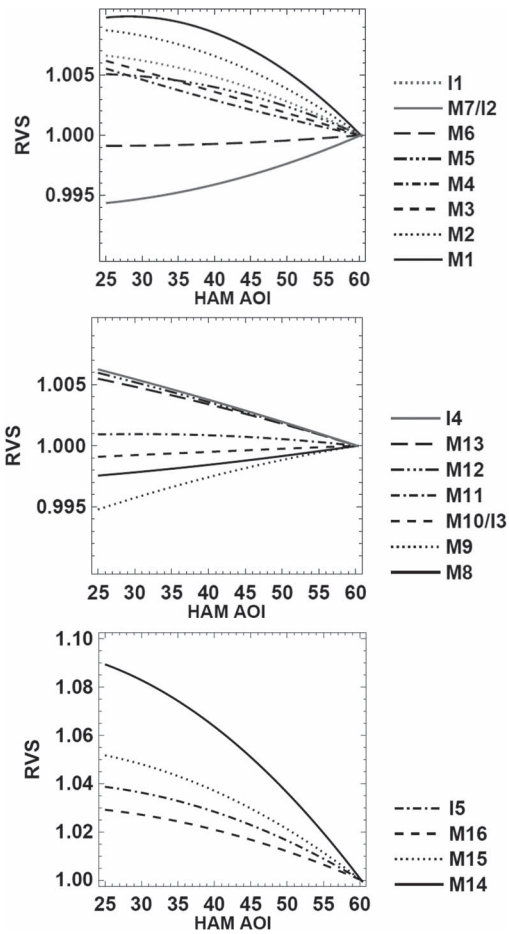

Fig. 7. VisNIR, SMWIR, and LWIR RVS functions.

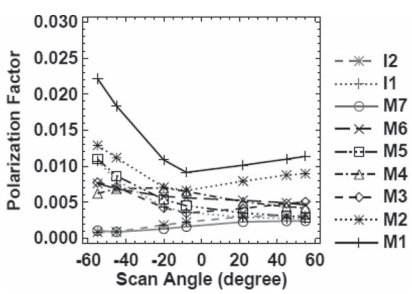

Fig. 8. VIIRS polarization for the VisNIR bands measured at seven scan angles.

MWIR RVS is generally small, varying by less than 1% over the full AOI range. In contrast, the LWIR RVS changes by up to 10% for M14 over the range of AOI. The TEB RVS uncertainty requirement was 0.2%, which was determined here as the fitting residuals; all TEB RVS uncertainties are lower than 0.1%, meeting the RVS characterization uncertainty requirement with a margin.

Polarization: The two-cycle amplitudes determined from the polarization sensitivity testing are plotted in Fig. 8 as a function of the scan angle for all VisNIR bands (band-averaged HAM side A). The polarization measurements had shown very high repeatability, and the uncertainty due to repeatability was smaller than 0.15% for all VisNIR bands. The largest polarization sensitivity occurred in band M1 at the beginning of the scan

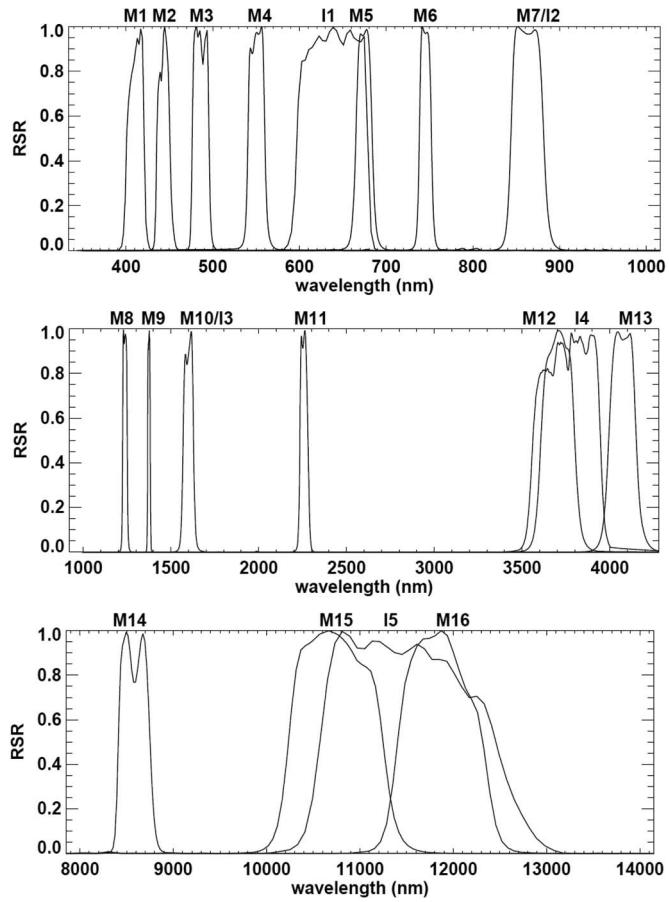

Fig. 9. VIIRS in-band RSRs for (top) VisNIR, (middle) SMWIR, and (bottom) LWIR bands.

but is still less than the 3% sensor specification (i.e., see Table II for specification values per band). The polarization sensitivity tends to be highly variable across the scan; the highest levels of polarized light on orbit are expected at the end of the scan for the S-NPP orbit. In addition, the polarization factors were observed to be detector dependent. At present, the root cause of this dependence has not been identified. In conclusion, the prelaunch polarization testing has shown that the VIIRS VisNIR bands are compliant with the polarization factor requirement with a significant margin, and the uncertainty of the derived polarization factors was less than the characterization uncertainty specification of 0.5%.

RSR: VIIRS spectral testing was performed in the TV environment at nominal plateau at sensor level for all bands and at ambient spacecraft level for the VisNIR bands only. Fig. 9 shows the in-band response for all VisNIR bands derived from sensor-level testing, and Fig. 10 shows the full band-average RSR for band M1, including OOB and optical crosstalk effects as measured using the T-SIRCUS. Using the insight from subject matter experts and a selection process based on SNR to identify the highest quality measurements, the VisNIR RSRs delivered to the SDR operational processing team were a combination of sensor-level testing and spacecraft-level testing. These RSRs are shown in the top plot of Fig. 9. The SWIR bands, which range in the band center from 1240 to 2250 nm, were tested from 1000 to 7100 nm in the TV environment only.

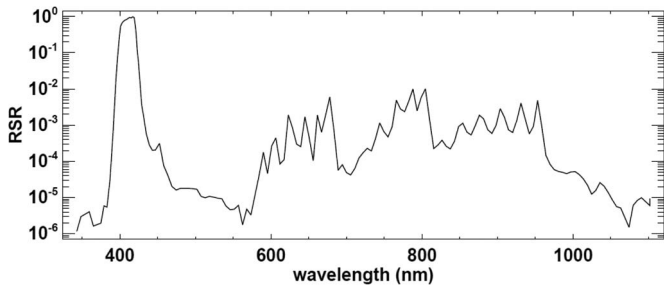

Fig. 10. RSR including the OOB for band M1.

The SWIR bands M8–M11 and I3 are shown as the middle plot on the left hand side of Fig. 9.

Compliance with the band center, bandwidth, extended bandpass, and integrated OOB (IOOB) requirements were calculated for all bands on a per detector basis. There were a few noncompliances in the RSB, and most of them are associated with the IOOB requirement. These IOOB noncompliances were exclusive to the VisNIR bands, and neglecting optical crosstalk, the following bands were noncompliant: M1, M3 (only a subset of the detectors), M4, M5, and M6. The largest noncompliances were in M4 and M5 which suffered from fluorescence in the filter material, but as the RSR was well characterized, none of the noncompliances were deemed a significant risk to SDR or EDR quality. Some other minor noncompliances included the M4 band center being slightly too short (i.e., 550.7 nm), the band M2 bandwidth being slightly short (i.e., 15.2 nm compared with 16 nm), and the band M8 bandwidth being slightly larger (i.e., 26.1 nm compared with 24 nm) than specification.

The TEB RSRs are shown in Fig. 9 for the MWIR bands M12, M13, and I4 (i.e., the right-hand side of the middle plot) and for the LWIR bands (i.e., lower plot). TEB spectral noncompliances were limited and not considered a risk to the SDR or EDR performance. Band M16 had a band center that was slightly out of compliance, 11 861 nm compared with a minimum of 11 925 nm. The only other in-band noncompliances were the bandwidth of band M14, which was 0.8 nm outside the bandwidth requirement, and band I5, which had a longer than specified extended bandpass. IOOB noncompliances were found in the bands M15, M16, and I5. All of these TEB noncompliances were minor and were considered a low risk to SDR and EDR performance.

Crosstalk: To help assess the impact of both the static and optical crosstalks, which have both failed the sensor requirement, crosstalk coefficients (ICs) characterizing the received crosstalk were produced for SDR and EDR impact assessments. The crosstalk ICs were computed separately for each one of VIIRS bands based on (20). A sample of a VIIRS IC map is shown for band M1 (412 nm) in Table V. This map represents the band average optical contamination into M1 from all other bands, including the M1 OOB contribution. Since the magnitude of VisNIR band optical crosstalk was of concern, an effort was made to assess its impact on the sensor SDR and a set of EDRs. The VisNIR IC map was then used to apply crosstalk ICs to representative MODIS scenes covering a wide range of anticipated on-orbit situations, including ocean, aerosol, land, and cloud scenes as stress tests. By applying algorithms based on VIIRS-equivalent spectral bands to MODIS data, it was possible to create rather realistic VIIRS data simulations that illustrate the anticipated VIIRS on-orbit performance [22]. The differences between the original scenes and the scenes with crosstalk added were taken as typical errors anticipated on orbit. These SDR crosstalk errors were analyzed by various science teams and deemed at acceptable levels for science products. Furthermore, the good image quality that the VIIRS instrument has observed since its launch is a good indication of very low crosstalk contamination.

VI. Summary

S-NPP VIIRS is the next generation of Earth-observing satellites capable of providing high-quality measurements to support a wide range of scientific and operational applications, including support for weather forecasting, and environmental monitoring and predictions. An intensive testing program was designed by the sensor contractor with support from the government calibration and science team. The instrument testing program was performed to characterize the radiometric, spectral, and spatial performance for all 22 spectral bands in various configurations and environments and simulating the range of on-orbit conditions. The key radiometric and spectral performances were discussed in this paper, including calibration methodologies, analysis results, and compliance with requirements. The VIIRS spectral band calibration and characterization have shown very good performance in terms of SNR, NEdT, dynamic range, gain transition, and linearity. The only exceptions are M8, which saturates at about 85% of the specified L_{MAX}, and the M13 dual gain band, which transitions slightly higher than the specification. The detector-to-detector uniformity was a very challenging requirement (uniformity less than the noise), and all of the low gain bands, as well as M10, M11, I1, and I2, failed this specification in certain portions of the dynamic range. The stray light and NFR performances were as expected, and all bands met the sensor requirements, except M11 due to stricter requirement and M15 and M16 which failed the NFR requirement by about 25%. The RVS functions derived for all bands have shown small variations over the full AOI range ($< 1\%$), with the exception of the LWIR, and a small variation between HAM sides except band M6. The polarization testing, performed using an enhanced setup, provided high-quality measurements and has shown compliance for all VisNIR bands with the polarization factor requirements as well as the characterization uncertainty requirements. The spectral measurements performed using the monochromator (TV) and the laser source (ambient) have allowed the high-quality measurement of the VisNIR RSRs, selecting and combining the best spectral response from each measurement. The SMWIR and LWIR RSRs were all derived using only the monochrometer measurements. There were a few spectral noncompliances associated with IOOB, the band center, and the bandpass, but none of these noncompliances were deemed a risk to SDR and EDR quality. Since the crosstalk requirements were extremely challenging and the testing is only representative of a uniform scene, the program opted to assess the crosstalk impact instead of requirement verification. A set of crosstalk coefficient maps

TABLE V
SAMPLE OF VCST CROSSTALK COEFFICIENT MAP DERIVED USING SPECTRAL DATA FOR M1 AS A RECEIVER AND ALL OTHER VISNIR BANDS AS SENDERS

	Sender Bands								
Spectral Bin	M1	M2	M3	M4	M5	M6	M7	I1	I2
340-402	0.00001034	0.00000308	0.00000004	-0.00000038	0.00000277	0.00000119	0.00000044	0.00000115	0.00000004
402-422	0.04999793	0.00347027	0.00058780	0.00095800	0.00015126	0.00012407	0.00012170	0.00024177	0.00015025
422-436	0.00025571	0.00000970	0.00000008	0.00000034	-0.00000010	-0.00000002	0.00000003	0.00000007	-0.00000001
436-454	0.00017750	0.00007455	0.00000148	0.00000370	0.00000048	0.00000097	0.00000039	-0.00000002	0.00000073
454-478	0.00002764	0.00000729	-0.00000065	0.00000345	-0.00000030	0.00000013	0.00000022	-0.00000007	-0.00000045
478-498	0.00001646	0.00000180	-0.00000775	0.00000438	0.00000046	0.00000027	0.00000007	0.00000067	-0.00000040
498-545	0.00002075	0.00000858	0.00000154	0.00002957	-0.00000011	0.00000085	-0.00000005	0.00000051	0.00000005
545-565	0.00000315	0.00000942	0.00000135	0.00004201	0.00000030	0.00000031	0.00000011	0.00000072	0.00000002
565-600	0.00007792	0.00000321	0.00000212	0.00003802	-0.00000021	0.00000012	-0.00000050	-0.00000043	-0.00000105
600-662	0.00216955	0.00005502	0.00001462	0.00009444	0.00000213	0.00000126	-0.00000062	-0.00000672	-0.00000838
662-682	0.00160772	0.00007158	0.00001342	0.00000185	-0.00001101	0.00000096	0.00000018	-0.00000025	-0.00000084
682-738	0.00027854	0.00000908	0.00000133	0.00000685	-0.00000025	0.00000878	0.00000005	0.00000087	-0.00000034
738-754	0.00050985	0.00001079	0.00000031	0.00000105	0.00000108	-0.00003574	0.00000024	0.00000061	0.00000005
754-845	0.01377604	0.00032950	0.00002005	0.00000996	0.00000327	0.00000494	0.00002644	0.00000190	0.00001527
845-885	0.00186800	0.00006393	0.00000267	0.00000216	0.00000333	-0.00000035	0.00014089	-0.00000396	0.00025599
885-1100	0.00657241	0.00019349	0.00001521	0.00000775	0.00000337	0.00000120	0.00001058	0.00000416	0.00000453

were derived from the test data and used in combination with a set of MODIS scenes to generate VIIRS-like crosstalk contaminated scenes. The crosstalk errors from these simulations were analyzed by the NASA science team for a select set of EDRs and confirmed the small impact on the quality of the SDR and EDR products.

In conclusion, the S-NPP VIIRS test program was completed successfully and provided a comprehensive test data set for sensor requirement verification, with many lessons learned for future JPSS VIIRS sensors. It also showed that the overall prelaunch sensor radiometric performance was of high quality. S-NPP VIIRS was launched on October 28, 2011, and as expected, it has been subsequently providing valuable SDRs to support science and environmental applications and programs.

ACKNOWLEDGMENT

The authors would like to thank the VIIRS team members from the Aerospace Corporation, the NASA Science Team, the NASA VIIRS Ocean Science Team, the University of Wisconsin, Massachusetts Institute of Technology Lincoln Laboratory, Raytheon, and Northrop Grumman for their valuable contributions to many of the VIIRS testing and performance verification. The authors would also like to thank the Moderate Resolution Imaging Spectroradiometer Characterization and Support Team as well as previous VIIRS Characterization Support Team members, who provided valuable support to the VIIRS program and to the prelaunch calibration and characterization effort.

REFERENCES

[1] T. F. Lee *et al.*, "NPOESS: Next-generation operational global earth observations," *Bull. Amer. Meteorol. Soc.*, vol. 91, no. 6, pp. 727–740, Jun. 2010.

[2] X. Xiong *et al.*, "VIIRS on-orbit calibration methodology and performance," *J. Geophys. Res.*, vol. 119, no. 9, pp. 5065–5078, May 2014.

[3] H. Oudrari *et al.*, "Preliminary assessment of Suomi-NPP VIIRS on-orbit radiometric performance," in *Proc. SPIE*, 2012, vol. 8510, p. 851036.

[4] X. Xiong *et al.*, "Early assessment of VIIRS on-orbit calibration and support activities," in *Proc. IEEE Int. Geosci. Remote Sens. Symp.*, Munich, Germany, 2012, pp. 7189–7192.

[5] W. L. Barnes and V. V. Salomonson, "MODIS: A global image spectroradiometer for the earth observing system," *Critical Rev. Opt. Sci. Technol.*, vol. CR47, pp. 285–307, 1993.

[6] C. McClain, S. Hooker, G. Feldman, and P. Bontempi, "Satellite data for ocean biology, biogeochemistry, climate research," *Eos Trans. AGU*, vol. 87, no. 34, pp. 337–339, Aug. 2006.

[7] M. D. King *et al.*, "Cloud and aerosol and water vapor properties, precipitable water, profiles of temperature and humidity from MODIS," *IEEE Trans. Geosci. Remote Sen.*, vol. 41, no. 2, pp. 442–458, Feb. 2003.

[8] C. O. Justice *et al.*, "The moderate resolution imaging spectroradiometer (MODIS): Land remote sensing for global change research," *IEEE Trans. Geosci. Remote Sen.*, vol. 36, no. 4, pp. 1228–1249, Jul. 1998.

[9] Northrop Grumman Aerospace System, "Joint Polar Satellite System (JPSS). VIIRS Radiometric Calibration Algorithm Theoretical Basis Document (ATBD)," Redondo Beach, CA, USA, Tech. Rep. D43777, Dec. 2010.

[10] X. Xiong, K. Chiang, J. Sun, W. Barnes, B. Guenther, and V. Salomonson, "NASA EOS Terra and Aqua MODIS on-orbit performance," *Adv. Space Res.*, vol. 43, no. 3, pp. 413–422, Feb. 2008.

[11] S. B. Hooker and C. R. McClain, "The calibration and validation of SeaWiFS data," *Progress Oceanography*, vol. 45, no. 3/4, pp. 427–465, Apr. 2000.

[12] C. Cao *et al.*, "Visible Infrared Imaging Radiometer Suite (VIIRS) Sensor Data Record (SDR) User's Guide," U.S. Dept. Commerce, Washington, DC, DC, USA, NOAA Tech. Rep. NESDIS 142, Sep. 2013.

[13] Goddard Space Flight Center, Joint Polar Satellite System (JPSS) VIIRS General Test Plan (GTP), Greenbelt, MD, USA, 2011.

[14] T. Scalione *et al.*, "Post-CDR NPOESS VIIRS sensor design and performance," in *Proc. SPIE*, 2004, vol. 5234, pp. 144–155.

[15] X. Xiong and W. Barnes, "An overview of MODIS radiometric calibration and characterization," *Adv. Atmos. Sci.*, vol. 23, no. 1, pp. 69–79, Jan. 2006.

[16] X. Xiong *et al.*, "Performance of Terra MODIS solar diffuser and solar diffuser stability monitor," in *Proc. SPIE*, 2005, vol. 5882, pp. 58820S-1–58820-10, doi: 10.1117/12.615334.

[17] Goddard Space Flight Center, "Joint Polar Satellite System (JPSS) VIIRS Reflective Solar Bands—Performance Verification Report (PVR)," Greenbelt, MD, USA, 2011.

[18] Goddard Space Flight Center, "Joint Polar Satellite System (JPSS) VIIRS Product Requirement Document (PRD)," Greenbelt, MD, USA, 2011.

[19] S. W. Brown, G. Eppeldauer, and K. R. Lykke, "Facility for spectral irradiance and radiance responsivity calibrations using uniform sources (SIRCUS)," *Appl. Opt.*, vol. 45, no. 32, pp. 8218–8237, Nov. 2006.

[20] C. Moeller, J. McIntire, T. Schwarting, and J. Costa, "Suomi NPP VIIRS spectral characterization: Understanding multiple RSR releases," in *Proc. SPIE , Earth Observ. Syst. XVII*, 2012, vol. 8510, pp. 85101S-1–85101S-15.

[21] L. B. Barnes, T. S. Pagano, and V. V. Salomonson, "Pre-launch characterization of the Moderate Resolution Imaging Spectroradiometer (MODIS) on EOS-AM1," *IEEE Trans. Geosci. Remote Sens.*, vol. 36, no. 4, pp. 1088–1100, Jul. 1998.

[22] H. Oudrari *et al.*, "A methodology to assess the impact of optical and electronic crosstalk in a new generation of sensors using MODIS heritage data," in *Proc. IEEE Int. Geosci. Remote Sens. Symp.*, Honolulu, HI, USA, 2010, pp. 2691–2694.

Hassan Oudrari received the M.Sc. degree in project management from George Washington University, Washington DC, USA, in 2014 and Ph.D. degree in physics of remote sensing from Denis Diderot University, Paris, France, in 2004.

He is a Chief Engineer at Sigma Space Corporation, Lanham, MD, USA, providing support to the Code 618 Biospheric Sciences Laboratory at NASA/Goddard Space Flight Center. He has worked in the field of remote sensing data calibration and image processing and supported multiple space missions such as the National Oceanic and Atmospheric Administration (NOAA)-Advanced High Resolution Radiometer, Landsat, Moderate Resolution Imaging Spectroradiometer, and Visible Infrared Imaging Radiometer Suite (VIIRS). His research includes sensor calibration and characterization as well as the use of radiative transfer for atmospheric correction. He was the NASA representative supporting the Suomi National Polar-orbiting Partnership VIIRS instrument prelaunch testing and characterization and postlaunch intensive calibration and validation. He is currently coordinating the NASA support to the Joint Polar-Orbiting Satellite System VIIRS development, working closely with the JPSS project management and sensor contractors and providing status on the sensor performance and issues.

Jeff McIntire, photograph and biography not available at the time of publication.

Xiaoxiong Xiong, photograph and biography not available at the time of publication.

Jim Butler received the B.S. degree in physical chemistry from the University of Notre Dame, Indiana, USA, in 1977 and the Ph.D. degree in physical chemistry from the University of North Carolina at Chapel Hill, Chapel Hill, NC, USA, in 1982.

He is an Optical Physicist in the Code 618 Biospheric Sciences Laboratory at NASA's Goddard Space Flight Center, Greenbelt, MD, USA. He has served as an Earth Observing System Calibration Scientist since 1995, Deputy S-NPP Project Scientist for Instruments and Calibration since 2004, and Joint Polar-Orbiting Satellite System Flight Project Scientist since 2011. He also serves as the Principal Investigator of the Code 618 Radiometric and Diffuser Calibration Laboratories. He is the NASA representative to the Executive Panel of the International Global Space-based Inter-Calibration System. His research experience includes the calibration and characterization of remote sensing instrumentation, optical metrology, ground-based and balloon-borne lidar for the detection of stratospheric molecular and radical species, laser-induced fluorescence of molecules and radicals, atomic and molecular spectroscopy, and photoionization and dissociation of molecules.

Shihyan Lee, photograph and biography not available at the time of publication.

Ning Lei received the B.S. degree in physics from Fudan University, Shanghai, China, in 1984 and the Ph.D. degree in physics from Rutgers University, The State University of New Jersey, New Brunswick, NJ, USA, in 1993.

He is a Scientist with the Visible Infrared Imaging Radiometer Suite (VIIRS) Characterization Support Team at Sigma Space Corporation, Lanham, MD, USA. He has worked on S-NPP VIIRS radiometric characterization and calibration since 2010. Before joining Sigma Space Corporation, he was a Scientist with the University of Chicago, IL, USA, engaged in both theoretical and experimental X-ray scattering studies of soft material structures and interactions.

Tom Schwarting, photograph and biography not available at the time of publication.

Junqiang Sun, photograph and biography not available at the time of publication.